

Tree tensor network state study of the ionic-neutral curve crossing of LiF

V. Murg¹, F. Verstraete¹, R. Schneider², P. R. Nagy³, and Ö. Legeza⁴

¹*Fakultät für Physik, Universität Wien, Boltzmannngasse 3, A-1090 Vienna, Austria*

²*Technische Universität Berlin Fakultät II - Mathematik und Naturwissenschaften
Institut für Mathematik, Strasse des 17. Juni 136, Berlin, Germany*

³*Eötvös Loránd University, Budapest, Pázmány P. sétány 1/A, H-1117, Hungary*

⁴*Strongly correlated systems "Lendület" research group,
Wigner Research Centre for Physics, P.O.Box 49 Hungary*

(Dated: June 20, 2021)

We present a tree-tensor-network-state (TTNS) method study of the ionic-neutral curve crossing of LiF. For this ansatz, the long-range correlation deviates from the mean-field value polynomially with distance, thus for quantum chemical applications the computational cost could be significantly smaller than that of previous attempts using the density matrix renormalization group (DMRG) method. Optimization of the tensor network topology and localization of the avoided crossing are discussed in terms of entanglement.

I. INTRODUCTION

It has been more than a decade ago that the quantum chemistry version of the density matrix renormalization group (QC-DMRG) method^{1,2} has been applied to study the ionic-neutral curve crossing of LiF in order to demonstrate that it provides a globally accurate description of the system even if the wavefunction changes dramatically transversing the avoided crossing³. In the following years, various theoretical studies have been devoted to investigate dissociation curves in diatomic molecules using QC-DMRG⁴⁻⁷ and by now the method has become a rival to the conventional multiconfiguration wave function approaches⁸⁻¹⁰. Inclusion of the concepts of entanglement from quantum information theory (QIT)¹¹⁻¹⁴ has paved the road for identifying highly correlated molecular orbitals leading to an efficient construction of active spaces^{11,15} and for characterizing the various types of correlation effects relevant for chemical bonding^{7,16}.

In the mean time, a reformulation of DMRG in terms of so-called matrix product states (MPS)¹⁷⁻²⁰ has shown that it is only one special case in a much more general set of methods: the so-called tensor network states (TNS)^{18,21-31}, which in certain cases is expected to even outperform QC-DMRG in the near future^{32,33}. A special form of TNS, the tree tensor network states (TTNS) approach³⁴⁻³⁷ was first applied in quantum chemistry by some of us³² to present the underlying theoretical background and scaling properties of the QC-TTNS algorithm while an efficient extension of the QC-DMRG using the tree-like topology has been applied recently to dendrimers³³. The TTNS approach also plays a fundamental role in *hierarchical tensor decompositions*, recently developed for tensor product approximation³⁰, see e.g.^{28,29}.

Unlike to models with translational symmetry studied usually in condensed matter physics, the orbital entanglement is non-constant in the quantum chemical applications. Therefore, the optimal arrangement of matrices in MPS-based approaches has a tremendous effect on their performance and on the required computational

resources to reach a given accuracy^{11,14,39}. Similar optimization strategies to find the best tensor topology are also crucial in case of the TTNS algorithm^{14,33}.

In this paper, we discuss the most general version of the QC-TTNS algorithm in which the local properties of the tensors can be different for each orbital. By studying the ionic-neutral potential curve crossing of the LiF we present an optimization strategy to set up tensor topologies which reflect the structure of the entanglement bonds between the molecular orbitals as the bond length between the Li and F is stretched. We also compare the MPS(DMRG) and TTNS convergence properties by changing the order of the tensors only. In our study, we calculate the two lowest $^1\Sigma^+$ states of LiF and the corresponding one- and two-orbital entropy functions^{7,13}. The localization of the avoided crossing in terms of orbital entropy is also discussed.

The setup of the paper is as follows. In Sec. II we briefly describe the main steps of the QC-TTNS algorithm and the details of the numerical procedure used to determine the optimal tensor arrangements. Sec. III contains the numerical results and analysis of the observed trends of the numerical error. The summary of our conclusions is presented in Sec. IV.

II. NUMERICAL PROCEDURE

A. Hamiltonian and target states

In the QC-DMRG and QC-TTNS applications, the electron-electron correlation is taken into account by an iterative procedure that minimizes the Rayleigh quotient corresponding to the Hamiltonian of the system:

$$H = \sum_{ij\sigma} T_{ij} c_{i\sigma}^\dagger c_{j\sigma} + \sum_{ijkl\sigma\sigma'} V_{ijkl} c_{i\sigma}^\dagger c_{j\sigma'}^\dagger c_{k\sigma'} c_{l\sigma}. \quad (1)$$

This Hamiltonian determines the exact states of the given molecule. In Eq. (1), $c_{i\sigma}^\dagger$ and $c_{j\sigma}$ creates and annihilates an electron with spin σ , respectively. T_{ij} denotes the

matrix elements of the one-particle Hamiltonian, which is comprised of the kinetic energy and the external electric field of the nuclei, and V_{ijkl} stands for the matrix elements of the electron repulsion operator, defined as

$$V_{ijkl} = \int d^3x_1 d^3x_2 \Phi_i^*(\vec{x}_1) \Phi_j^*(\vec{x}_2) \frac{1}{|\vec{x}_1 - \vec{x}_2|} \Phi_k(\vec{x}_2) \Phi_l(\vec{x}_1).$$

The matrix elements T_{ij} and V_{ijkl} are expressed in a molecular orbital (MO) basis obtained by CASSCF optimizations. The benchmark energies are computed with the same set of MO's. (For more details, see section Basis states.)

In the present version of our TTNS method non-Abelian symmetries⁴⁰⁻⁴⁴ are not implemented yet, thus in order to specify the eigenstates we have fixed the number of electrons with up and down spins and shifted the triplet levels from the low lying spectrum by adding a term $\sum_{i,j} \delta (S_i^+ S_j^- + S_i^- S_j^+)$ with $S_i^+ = c_{i\sigma}^\dagger c_{j\sigma'}$ and $\delta = 1$ to the Hamiltonian given in Eq. (1). Nevertheless, we have also checked the total spin of each states by calculating the expectation value of the $S^2 = \sum_{ij} S_i^- S_j^+ + \sum_{ij} S_i^z S_j^z + \sum_i S_i^z$ operator which is equal to $S(S+1)$ in Hartree atomic units, i.e., zero for a singlet state and two for a triplet state.

In the MPS-based approaches, several eigenstates can be calculated within a single calculation. Therefore, we have formed the reduced density matrix of the target state, ρ , from the reduced density matrices of the lowest n eigenstates as $\rho = \sum_\gamma p_\gamma \rho_\gamma$ with $\gamma = 1 \dots n$ and $p_\gamma = 1/n$ at each bond length. In case of our QC-DMRG code the orbital spatial symmetry of the target state can also be fixed³⁹ in which case the first two lowest lying $^1\Sigma^+$ states can be calculated directly by using only $n = 2$ eigenstates of the related subspace of the Hamiltonian. In the present version of our TTNS method, however, orbital spatial symmetry is not implemented yet. Therefore, we had to target the four lowest lying states with $n = 4$ due to the fact that there are two additional eigenstates between the two lowest $^1\Sigma^+$ states. For more detailed descriptions of target states we refer to the original works and reviews^{1,3,45}.

B. Basis states

Atomic orbital (AO) basis was adopted from the work of Bauschlicher and Langhoff⁴⁶ in order to match with previous DMRG computations³. The AO basis set of Ref.⁴⁶ is suitable to describe the ionic and covalent LiF states as well. It consists of 9s and 4p functions contracted to 4s and 2p functions on the Li atom and 9s, 6p and 1d functions contracted to 4s, 3p and 1d on the F atom. For more details of the AO basis set we refer to the original publication⁴⁶.

The two lowest $^1\Sigma^+$ states of LiF around the equilibrium bond length can be qualitatively described by the $1\sigma^2 2\sigma^2 3\sigma^2 4\sigma^2 1\pi^4$ and $1\sigma^2 2\sigma^2 3\sigma^2 4\sigma^1 5\sigma^1 1\pi^4$

configurations⁴⁶. For this reason, the MO basis was obtained by CASSCF optimizations, with two active electrons on two active orbitals (4 σ and 5 σ) (CAS(2,2)). MO's were optimized simultaneously for both $^1\Sigma^+$ states. T_{ij} and V_{ijkl} matrix elements of Eq. (1) are expressed in this MO basis. CASSCF optimizations were carried out with the GAMESS quantum chemistry package⁴⁷.

Orbitals 1 σ , 2 σ and 3 σ were kept frozen in all presented configurational interaction (CI), MPS(DMRG) and TTNS computations. Six of the valence electrons were excited to all orbitals in the CI calculation, which we use as reference to compare the TTNS results to. CI results were obtained by utilizing the determinant-based full-configuration interaction (full-CI) program of Z. Rolik (Budapest), which is based on the CI algorithm of Olsen et al.⁴⁸. C_{2v} point group symmetry constraints were assigned during this study.

C. The QC-TTNS method

In this section, we present the brief overview of the most general QC-TTNS algorithm. For the full description of the method we refer to the original work³². In our implementation, we allow tensors to have orbital dependent coordination number, z_i , in contrast to the implementation of Nakatani *et. al.*³³ which is an efficient extension of the DMRG method using fixed number of blocks. Our main motivation is to develop an algorithm which reflects the entanglement structure of the molecule under study as much as possible (see Fig. 8). The computational cost in one step of the algorithm scales as D^{z_i+1} where D is the dimension of the auxiliary space (in the DMRG community referred as block states) while the the long-range correlation deviates from the mean-field value only polynomially with distance. Therefore, there is a trade-off between entanglement localization and increased order of the tensors. The construction of the optimal tensor network is thus a far more complex task than it is in case of the MPS based approaches.

In a full-CI treatment, a given eigenfunction of Eq. (1) can be written in a full tensor form as

$$|\Psi\rangle = \sum_{\alpha_1, \dots, \alpha_N} U_{\alpha_1 \dots \alpha_N} |\alpha_1, \dots, \alpha_N\rangle. \quad (2)$$

where $U_{\alpha_1 \dots \alpha_N}$ is a tensor with order N and $|\alpha_i\rangle$ represents basis states at molecular orbital i . In our study, a molecular orbital can be empty, singly occupied with up or down spins or doubly occupied, thus the dimension of the local Hilbert space, d , is four. Since the number of independent parameters in U scales exponentially with N it is mandatory to approximate such high dimensional tensor with a proper factorization in terms of lower dimensional tensors. In the MPS representation, U describes a matrix network, i.e., it emerges from contractions of a set of matrices $\{A^1, \dots, A^N\}$, where

$$A^i [\alpha_i]_{m_{i-1}, m_i}, \quad (3)$$

is a matrix at each vertex i of the network, with 2 virtual indices m_{i-1}, m_i of dimension D and one physical index α_i of dimension d , thus

$$|\Psi\rangle = \sum_{\alpha_1, \dots, \alpha_N} A_{\alpha_1}^1 A_{\alpha_2}^2 \dots A_{\alpha_N}^N |\alpha_1\rangle |\alpha_2\rangle \dots |\alpha_N\rangle. \quad (4)$$

The schematic plot of the matrix product state (MPS) network is shown in Fig. 1.

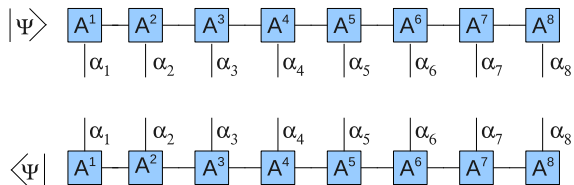


FIG. 1. (Color online) Schematic plot of the matrix product state (MPS) algorithm. Each node is represented by a tensor of order 2 and the vertical line the physical index α .

A natural extension of the MPS approach is to use higher order tensors. In this work, we form a tree tensor network in which all sites in the tree represent physical orbitals and in which entanglement is transferred via the virtual bonds that connect the sites as shown in Fig. 2. Our motivation is to treat models in which orbitals have

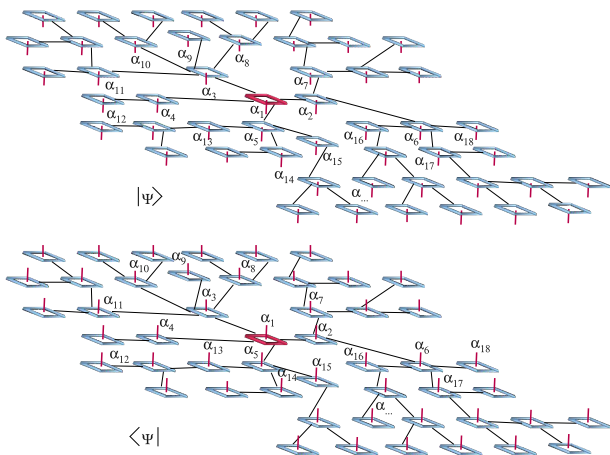


FIG. 2. (Color online) Schematic plot of a higher dimensional network, for example, the tree tensor network state (TTNS) algorithm. Each node is represented by a tensor of order z_i , where z_i is an orbital dependent coordination number. The network supposed to reflect the entanglement structure of the molecule as much as possible. The vertical red lines denote physical indices α_i , $i \in \{1, N\}$. Entanglement is transferred via the virtual bonds that connect the orbitals shown by black lines. The central node is indicated by red contour.

varying degrees of entanglement; positions closer to the center of the tree should be better suited to represent more entangled sites. An additional motivation is to take advantage of the property of the tree tensor network ansatz that the long-range correlations differ from

the mean-field value polynomially with distance rather than exponentially with distance as for MPS. In our algorithmic approach to optimize the tree tensor network, we use tools similar to those used in Refs. [34], [35], [36], and [37], and optimize the network site-by-site as in the DMRG. Therefore, $U_{\alpha_1 \dots \alpha_N}$ can describe a tree tensor network, i.e., they emerge from contractions of a set of tensors $\{A_1, \dots, A_N\}$, where

$$A^i[\alpha_i]_{m_1 \dots m_z}, \quad (5)$$

is a tensor with $z+1$ indices, at each vertex i of the network according to Fig. 3. Each tensor has z virtual indices $m_1 \dots m_z$ of dimension D and one physical index α_i of dimension d , with z being the coordination number of that site. The coefficients $U_{\alpha_1 \dots \alpha_N}$ are obtained by contracting the virtual indices of the tensors according to the scheme of a tree tensor network (see Fig. 3). The structure of the network can be arbitrary and the coordination number can vary from site to site. The only condition is that the network is bipartite, i.e., by cutting one bond, the network separates into two disjoint parts. Therefore, the TTNS network does not contain any loop (see Fig. 3) which allows an exact mathematical treatment^{28,30}. For $z=2$, the one-dimensional MPS-ansatz used in DMRG is recovered.

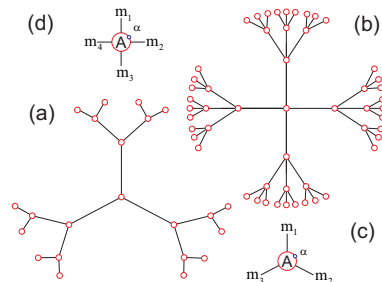


FIG. 3. (Color online) Top view of the tree tensor network (TTNS) algorithm with fixed coordination number, (a) $z_i = 3$, and (b) $z_i = 4$. The structure of the tensors is shown in (c) and (d). The bonds indicate the virtual indices m_1, \dots, m_z and the circle the physical index α .

Since entanglement is transferred via the virtual bonds that connect the sites, it is preferable to put strongly correlated sites close together, i.e. to minimize the number of bonds between them. For $z > 2$ the number of virtual bonds required to connect two arbitrary orbitals scales logarithmically with the number of orbitals α , whereas the scaling is linear in N for $z=2$. This can be seen by considering a Cayley-tree of depth Δ , as shown in Fig. 3. The number of sites in the tree is

$$N = 1 + z \sum_{j=1}^{\Delta} (z-1)^{j-1} = \frac{z(z-1)^{\Delta} - 2}{z-2}$$

and thus, the maximal distance between two orbitals, 2Δ , scales logarithmically with N for $z > 2$. Because of

this logarithmic scaling, the expectation value of a long-range correlations differs from the mean-field result by a quantity that scales polynomially with distance. This contrasts the MPS ansatz ($z = 2$) that shows an exponential decay of the difference with distance.³²

The TTNS algorithm consists in the variational optimization of the tensors A_i in such a way that the energy is minimized (with the constraint that the norm of the state remains constant). This is equivalent to optimizing the functional

$$F = \langle \Psi | H | \Psi \rangle - E (\langle \Psi | \Psi \rangle - 1),$$

where $\Psi = \Psi(A_1, \dots, A_N)$. This functional is non-convex with respect to all parameters $\{A_1, \dots, A_N\}$. However, fixing all tensors A_k except A_i , due to the tensor network structure of the ansatz, it is quadratic in the parameters A_i associated with one lattice site i . Because of this, the optimal parameters A_i can simply be found by solving a generalized eigenvalue problem $\mathcal{H}_i \vec{A}_i = E \mathcal{N}_i \vec{A}_i$. For a bipartite network, it is always possible to assume a gauge condition so that $\mathcal{N}_i = \mathbb{1}$, and thus reduce the generalized eigenvalue problem to an ordinary one.³² The concept of the algorithm is to do this one-site optimization site-by-site until convergence is reached. The challenge that remains is to calculate the effective Hamiltonian \mathcal{H}_i of the eigenvalue problem. In principle, this is done by contracting all indices in the expression for the expectation value $\langle \Psi | H | \Psi \rangle$ except those that connect to A_i . By interpreting the tensor A_i as a qD^z -dimensional vector \vec{A}_i , this expression can be written as $\langle \Psi | H | \Psi \rangle = \vec{A}_i^\dagger \mathcal{H}_i \vec{A}_i$. Since $\langle \Psi | \Psi \rangle = \vec{A}_i^\dagger \mathcal{N}_i \vec{A}_i$ and $\mathcal{N}_i = \mathbb{1}$, the functional F attains its minimum when

$$\mathcal{H}_i \vec{A}_i = E \vec{A}_i.$$

Due to the bipartite structure of the tensor network, the calculation of \mathcal{H}_i can be performed efficiently, i.e., on a time that scales polynomially with N and D .

This TTNS algorithm is similar to a DMRG calculation with z blocks instead of two, where a block consists of all of the sites within one of the branches emerging from site i (see Fig. 4(a)). The wave function is then formed as

$$|\Psi\rangle = \sum_{m_1, \dots, m_z=1}^D |\varphi_{m_1 \dots m_z}\rangle \otimes |\phi_{m_1}^1\rangle \otimes \dots \otimes |\phi_{m_z}^z\rangle, \quad (6)$$

where $|\phi_m^\gamma\rangle$ ($m = 1, \dots, D$) is the basis in environment block γ ($\gamma = 1, \dots, z$) and $|\varphi_{\alpha_1 \dots \alpha_z}\rangle$ is the state of site i . Matrix \mathcal{N}_i is equal to the identity if the basis $|\phi_m^j\rangle$ in each environment block is orthonormal. This can always be achieved, because of a gauge degree of freedom in a TTNS^{20,32,38}: it is possible to insert at any bond a resolution of the identity $\mathbb{1} = VW$, and contract the matrices V and W with the adjacent tensors A_i (see Fig. 4b). This does not change the state, but changes the tensors A_i and the basis states $|\phi_m^j\rangle$ of the environment blocks. It can be shown that it is always possible to find gauge

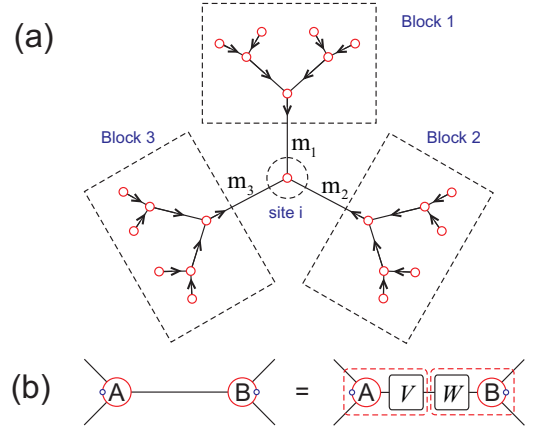


FIG. 4. (Color online) (a) Separation of the state into z blocks plus the site under optimization, as described by Eq. (6). (b) Natural freedom in the tensor network: insertion of a matrices V and W fulfilling $VW = 1$ at one bond leaves the state invariant. The contraction of A with V forms the new tensor A' on the left hand side; the contraction of B with W forms the new tensor B' at the right hand side.

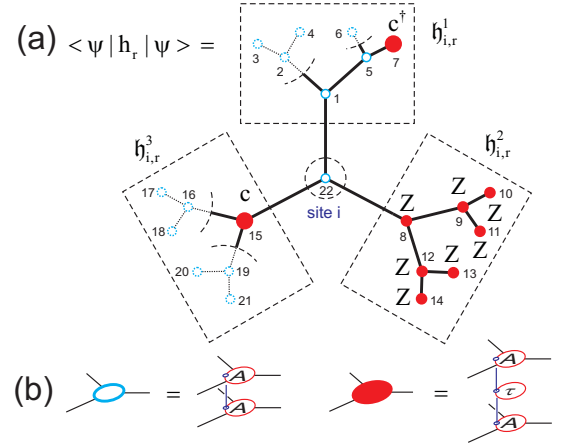


FIG. 5. (Color online) Formation of the effective Hamiltonian $\mathfrak{h}_{i,r} = \mathfrak{h}_{i,r}^1 \otimes \mathfrak{h}_{i,r}^2 \otimes \mathfrak{h}_{i,r}^3$ with respect to the fermionic interaction $h_r = c_7^\dagger c_{15}$. Between sites 7 and 15 a chain of Z -matrices appears due to the Jordan-Wigner transformation. The sites on which the interaction has support are marked in red. Each open (filled) circle in the tensor network corresponds to the contraction of the layered structure of tensors shown in (b).

transformations that orthonormalize the basis states of the environment blocks.³²

Thus, by assuring that the gauge condition is always satisfied in the course of the algorithm, the only term that must be calculated is the effective Hamiltonian \mathcal{H}_i . This term is obtained by contracting all tensors except A_i in the expectation value $\langle \Psi | H | \Psi \rangle$. Hamiltonian H

is a sum of $O(N^4)$ two-point and four-point fermionic interaction terms $c_{i\sigma}^\dagger c_{j\sigma}$ and $c_{i\sigma}^\dagger c_{j\sigma'}^\dagger c_{k\sigma'} c_{l\sigma}$ ($\sigma, \sigma' \in \{\uparrow, \downarrow\}$), as defined in eq. (1). The fermionic nature of the terms can be handled by mapping them to non-local bosonic operators via Jordan-Wigner transformations. Writing $H = \sum_r h_r$ with h_r denoting the Jordan-Wigner transformed two and four-point interaction terms, the effective Hamiltonian \mathcal{H}_i transforms into a sum $\mathcal{H}_i = \sum_r \mathfrak{h}_{i,r}$, where

$$\langle \Psi | h_r | \Psi \rangle = \vec{A}_i^\dagger \mathfrak{h}_{i,r} \vec{A}_i.$$

Due to the structure (6) of the TTNS, each effective Hamiltonian $\mathfrak{h}_{i,r}$ factorizes into a tensor product of z matrices

$$\mathfrak{h}_{i,r} = \mathfrak{h}_{i,r}^1 \otimes \cdots \otimes \mathfrak{h}_{i,r}^z,$$

where each matrix $\mathfrak{h}_{i,r}^\gamma$ corresponds to the matrix elements of h_i with respect to the basis in environment block γ :

$$[\mathfrak{h}_{i,r}^\gamma]_{mn} = \langle \phi_m^\gamma | h_r | \phi_n^\gamma \rangle.$$

Graphically, the evaluation of $\langle \phi_m^\gamma | h_r | \phi_n^\gamma \rangle$ corresponds to the contraction of a three-layered tensor network according to the structure of the branch in block γ , as depicted in Fig. 5. This network can be contracted efficiently by starting from the leaves and working in the inward direction.

With TTNS we can easily enforce the $U(1)$ symmetry that is fulfilled by Hamiltonian (1), i.e. the conservation of the number of particles. For this, the tree graph has to be made directed (see Fig. 4a), such that all sites (except site i that is optimized) have $z-1$ incoming and one outgoing bond. Thus, each virtual index of a tensor A_i is equipped with the additional information of whether it is “incoming” or “outgoing”. Each virtual index connecting to block γ ($\gamma = 1, \dots, z$) is split into an index tuple $(m_\gamma, n_\gamma^\uparrow, n_\gamma^\downarrow)$. Assuming that the index connecting to block $\gamma = 1$ is the outgoing index, we require that $n_1^\uparrow = n_2^\uparrow + \dots + n_z^\uparrow + n^\uparrow(\alpha)$ and $n_1^\downarrow = n_2^\downarrow + \dots + n_z^\downarrow + n^\downarrow(\alpha)$. $n^\uparrow(\alpha)$ ($n^\downarrow(\alpha)$) denotes the number of electrons with spin up (down) corresponding to the physical index α . Thus, for $\gamma = 2, \dots, z$, n_γ^\uparrow (n_γ^\downarrow) counts the number of up-electrons (down-electrons) within branch γ . The index n_1^\uparrow (n_1^\downarrow), on the other hand, is equal to the number of electrons with spin up (down) in all the branches plus the number of electrons at site i .

Besides the ability of targeting a state with a specific total number of up- and down-electrons N_\uparrow and N_\downarrow and giving a performance boost to the algorithm (the virtual dimension effectively increases from D to $D(N_\uparrow+1)(N_\downarrow+1)$), the inclusion of the particle-number conservation also simplifies the treatment of the fermionic nature of the electrons. The main idea is depicted in Fig. 6 for the interaction $c_\gamma^\dagger c_{15}$: with an appropriately chosen numbering of the fermions, each subbranch that has no fermionic support either has only identities acting on the sites

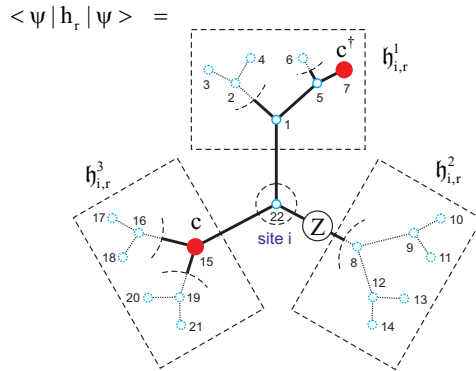


FIG. 6. (Color online) Formation of the effective Hamiltonian $\mathfrak{h}_{i,r} = \mathfrak{h}_{i,r}^1 \otimes \mathfrak{h}_{i,r}^2 \otimes \mathfrak{h}_{i,r}^3$ with respect to the fermionic interaction $h_r = c_\gamma^\dagger c_{15}$ with particle number conservation taken into account. The sites on which the interaction has support are marked in red. All branches marked by dotted lines and circles yield the identity when contracted. The parity operator \tilde{Z} is contracted to the virtual bond.

or only matrices Z stemming from the Jordan-Wigner transformation ($Z_{\alpha\beta} = \delta_{\alpha\beta}(-1)^{n^\uparrow(\alpha)+n^\downarrow(\alpha)}$). The subbranches including only identities simplify to the identity because we work in a gauge in which the basis in each environment block is orthonormal. As shown in [32], the Z operators can be “moved” to the virtual bonds and, since $Z^2 = \mathbb{1}$, all of them except one cancel (see Figs. 5 and 6). What remains is a subbranch that includes only identities, which reduces to the identity because of the orthonormalization of the state. Thus, for a fermionic two-site interaction, it is sufficient to take into account the path connecting the two sites. In this way, the treatment of long-range fermionic interactions is feasible with the same numerical effort as the treatment of long-range spin interactions.

The numerical effort of the algorithm has two major contributions. On the one hand, the bond-dimension D is crucial: the numerical effort for calculating one term of the effective Hamiltonian by tensor contraction scales as D^{z+1} . On the other hand, this calculation has to be performed for each term in the Hamiltonian, such that naively a scaling $N^4 D^{z+1}$ is expected. Fortunately, the same summation tricks as described in [2] can be applied, such that the scaling reduces to $N^2 D^{z+1}$. Since $O(N)$ iteration steps are required for convergence, the overall time of the algorithm will scale as $N^3 D^{z+1}$.

D. Network optimization by entanglement localization

The amount of contribution to the total correlation energy of an orbital can be detected qualitatively by the

single-orbital entropy, $s(1)_i = -\text{Tr}\rho_i \ln \rho_i$ where ρ_i is the reduced density matrix at orbital i . The two-orbital entropy is constructed similarly using the reduced density matrix, ρ_{ij} of a subsystem built from orbitals i and j and the mutual information $I_{ij} = s(2)_{ij} - s(1)_i - s(1)_j$ describes how orbitals are entangled with each other as they are embedded in the whole system. For more detailed derivations we refer to the original papers^{7,11,13,14}. Therefore, these quantities provide chemical information about the system, especially about bond formation and nature of static and dynamic correlation^{7,15,16,54}. As an example, $s(1)_i$ and I_{ij} are shown in Figs. 7 and 8, respectively, for the equilibrium bond length $r = 3.05$ and at large separation $r = 13.7$. The total quantum infor-

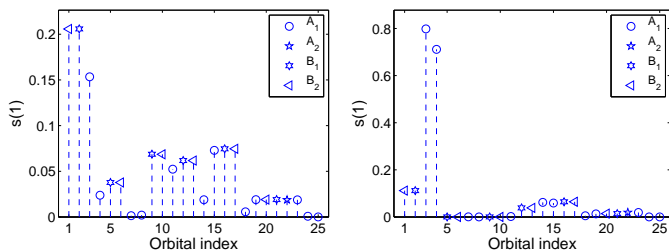


FIG. 7. (Color online) One orbital entropy profile for the LiF molecule at bond length (a) $r = 3.05$ and at (b) $r = 13.7$. Symbols label the irreducible representations of the molecular orbitals in the C_{2v} point group.

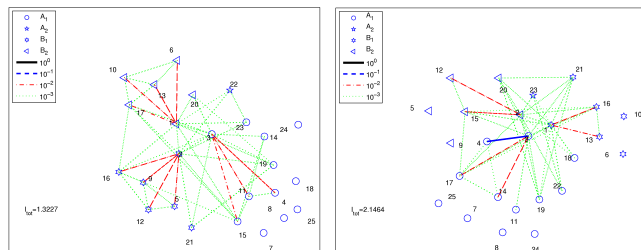


FIG. 8. (Color online) Mutual information represented as a two-dimensional weighted graph for the LiF molecule at bond length (a) $r = 3.05$ and at (b) $r = 13.7$. Colors indicate different strengths of I_{ij} and the symbols label the irreducible representations of the molecular orbitals in the C_{2v} point group.

mation encoded in the wavefunction is given by the sum of the orbital entropy, i.e., $I_{\text{tot}} = \sum_i s(1)_i$ which is twice as large for the stretched geometry as compared to the equilibrium case.

It is clear from Fig. 8 that some orbitals are strongly entangled with several other orbitals while some orbitals are entangled with only a few others and some are almost disentangled from the system. Therefore, the obvious choice is to allow the coordination number, z_i , to vary from orbital to orbital. In the following analysis, however, we restrict ourselves to a fixed $z_i = 3$ case in order to allow a more direct analysis when data are compared to the $z_i = 2$ MPS case.

Since both DMRG and TTNS rely on the systematic application of the Schmidt-decomposition the required computational resources to reach a given error margin is determined by the amount of entanglement in the system³⁹. This can be manipulated by changing the basis functions^{32,49} or by changing the tensor topology. For the latter case, the entanglement length,

$$\text{Cost}_\eta = \sum_{ij} I_{ij} \times d_{ij}^\eta, \quad (7)$$

should be minimized in order to localize the entanglement in the system, where d_{ij} is the distance function between orbital i and j depending on the tensor topology and η is some exponent that we set to 1 or 2. For the one-dimensional case, i.e., for DMRG and MPS $d_{ij} = |i - j|$. For the tree topology d_{ij} can be computed as the distance from the center to i , plus the distance from the center to j , minus twice the distance from the center to their lowest common ancestor. The lowest common ancestor can be obtained within a linear preprocessing time $O(N)$ and a constant query time using the Berkman's algorithm.⁵⁵ As an example, the optimized tensor topologies at the equilibrium bond length $r = 3.05$ are shown in Figs. 9 for the one-dimensional topology and for the tree topology.

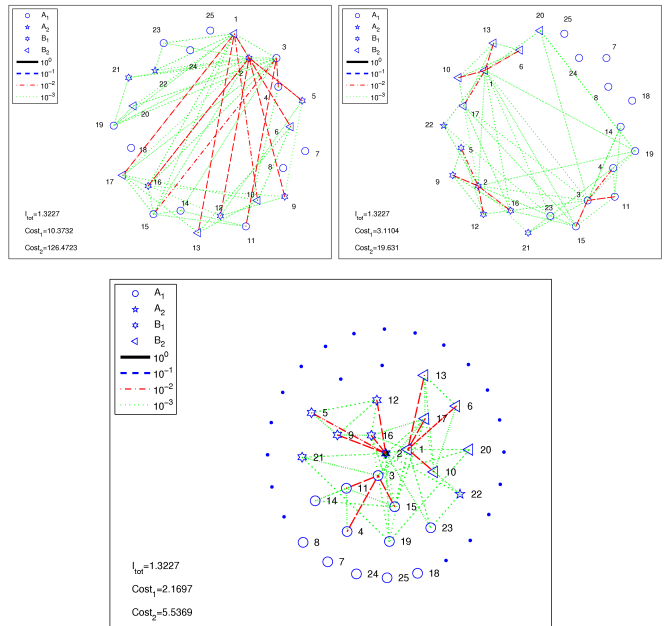


FIG. 9. (Color online) Optimization of tensor topology by minimizing the entanglement length in the system at the equilibrium bond length $r = 3.05$. (a) and (b) are for the one dimensional MPS like topology for the original ordering and for the optimized ordering, respectively. (c) Shows the optimized topology on the tree (small dots indicate not used grid points of the tree). The total quantum information I_{tot} does not change but the entanglement length calculated with $\eta = 1$ and 2 indicated by Cost_1 and Cost_2 drops significantly.

In practice, first we performed a quick and fast DMRG full sweep with a fixed small number of block states

($M \simeq 16, \dots, 64$) using the ordering of orbitals for which the T_{ij} and V_{ijkl} integral files were generated by the GAMESS program in order to determine the one and two-orbital entropy profiles qualitatively. For all subsequent calculations we rendered orbitals with descending orbital entropy values to form the Complete Active Space CAS-vector that was used during the configuration interaction based dynamic extended active space (CI-DEAS) procedure¹¹. We also determined the mutual information, I_{ij} , and the orbitals were reordered by minimizing the entanglement length given by Eq. (7). In the one-dimensional case either the graph Laplacian can be used or by other heuristic methods to reduce the spectral envelope of I_{ij} , i.e., to make it as diagonally dominant as possible^{50,51}. In case of the tree network, the optimization is less straightforward, but as a rule of thumb we placed orbitals with largest entropy values close to the center of the network while keeping orbitals with large I_{ij} values close together (see Fig. 9(c)). In the subsequent step, accurate DMRG (with optimized CAS vector) or MPS/TTNS calculations were performed.

III. NUMERICAL RESULTS

A. Ground state and excited states

In this work we have used two codes. Our QC-DMRG program has been developed for a long time and it includes advanced features like the dynamic block state selection (DBSS) approach^{12,39}, the CI-DEAS procedure¹¹, and the treatment of orbital spatial symmetries which are not implemented yet in the TTNS code. Therefore, the entropy functions were calculated by the QC-DMRG code to provide initial data quickly for network optimizations. The rest of the analysis for a fair treatment is, however, based on the TTNS code alone using fixed $z_i = 2$ (MPS) and $z_i = 3$ (TTNS) coordination number while keeping all other parameters of the algorithm the same.

The potential energy curve (PES) can be calculated for an a priori set error margin using the DBSS procedure³. Therefore, we have easily reproduced the full-CI energies up to 10^{-8} a.u. in absolute error. In the following, however, we have used a small fixed number of block states, i.e., fixed bond dimension, in order to demonstrate the benefits underlying the TTNS geometry. The four lowest lying eigenstates ($\gamma = 1, \dots, 4$) are shown in Fig. 10 calculated by the QC-DMRG method using $M = 16$ block states or alternatively by the TTNS approach with $z_i = 2$ and $D = 4$. We have confirmed that each state is a singlet with $S^2 = 0$.

The relative error of the ground state ($\gamma = 1$) and the third excited state ($\gamma = 4$), $\Delta E_\gamma = |E_\gamma - E_{\text{FCI},\gamma}|/E_{\text{FCI},\gamma}$, are shown in Fig. 11. The open symbols stand for the MPS solution while the filled symbols indicate the TTNS result. It is clear from the figure that the accuracy of the energy dropped for both states by at least an order of magnitude. For the ground state close to the equilibrium

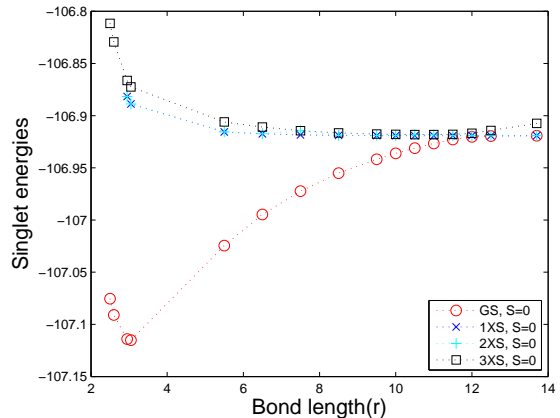


FIG. 10. (Color online) The energy of the four lowest lying states as a function bond length.

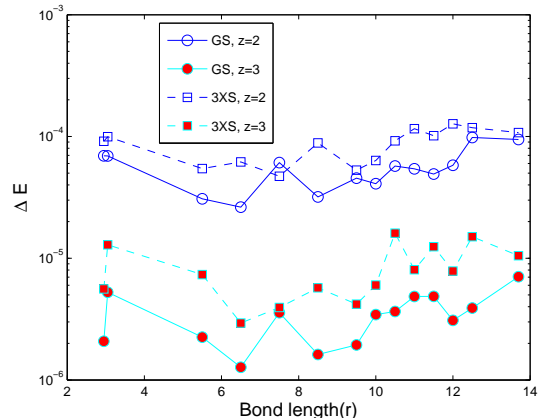


FIG. 11. (Color online) The relative error of the energy of the two lowest lying $^1\Sigma^+$ states as a function of bond length using the Tree-TNS with $z = 2$ and $z = 3$ with $D = 4$. For $z = 2$, the one-dimensional MPS-ansatz used in DMRG is recovered.

bond length the change is almost two orders of magnitude. It is important to emphasize again that all parameters of the calculations were kept fixed except that we used the optimized one-dimensional MPS-like topologies or the two-dimensional optimized TTNS-like topologies. The network topologies for both cases were optimized for each bond length using the procedure outlined in Sec. II.

In the MPS based DMRG method the matrices of the one-dimensional tensor network are optimized iteratively by traversing through the network starting from the left boundary until the right boundary is reached. In the following steps the same procedure is repeated but in the reverse direction. This systematic optimization procedure is called as sweeping. The relative error of the two $^1\Sigma^+$ states as a function of iteration steps is shown in Fig. 12 for the MPS case with $z_i = 2$ and $D = 4$. It can be seen in the figure that the relative error of the ground state energy drops quickly as a function of iteration steps

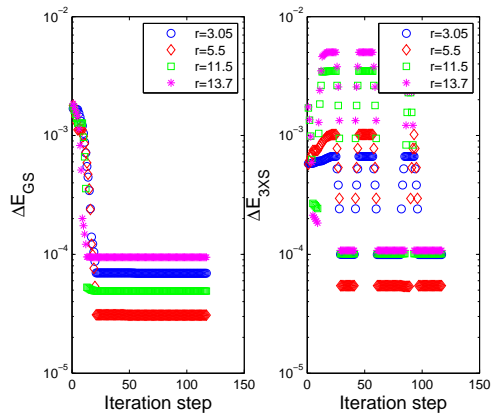


FIG. 12. (Color online) The relative error of the energy of the ground state and the third excited state as a function of iteration step with $z_i = 2$ and $D = 4$ for a few selected bond lengths.

and it saturates after some 20 iterations. In contrast to this, the convergence of the third excited state is somewhat slower. In addition, the method lost the target state for certain interaction steps, i.e., for certain network configurations. This is due to the very low bond dimension used in the test calculations. When we used larger bond dimension or included point group symmetries this problem was fully eliminated.

In case of the tree-network, there is more freedom to choose the optimal sweeping procedure, i.e., to choose the optimal path through which the network is traversed. In the present work, we have swept through the network by going recursively back and forth through each branch. Therefore, according to the labeling of the orbitals on the lattice shown in Fig. 13 one sweep goes through the orbitals as 1 2 3 4 5 4 6 4 3 7 8 7 3 2 9 10 9 11 9 2 1 12 13 14 13 15 13 12 16 17 16 18 16 12 1 19 20 21 20 22 20 19 23 24 23 25 23 19. The main advantage of

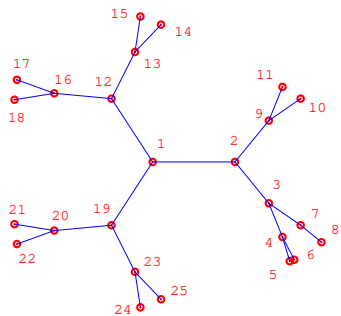


FIG. 13. (Color online) The figure shows how the tree network is traversed through in a full sweep.

this path is that highly entangled orbitals located close to the center of the network are optimized several times in a full sweep. The relative error of the two $^1\Sigma^+$ states

as a function of iteration steps obtained by the TTNS method with $z_i = 3$ and $D = 4$ is shown in Fig. 14. It

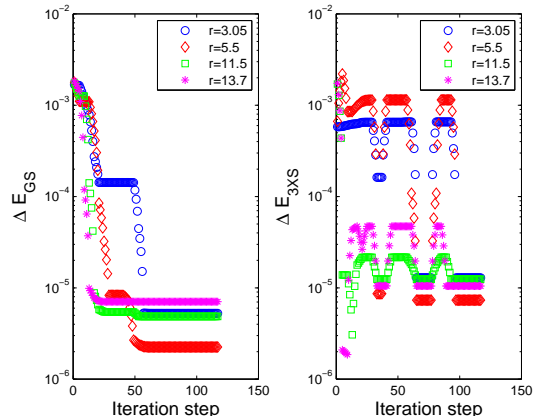


FIG. 14. (Color online) Similar to Fig. 12 but for the TTNS method with $z = 3$.

can be seen that the relative error of the ground state energy reached the saturation value of the MPS calculation (shown in Fig. 12) after a few iteration steps. However, unlike to the MPS result the error dropped further for subsequent iteration steps until a much lower saturation value was reached. The overall improvement compared to the MPS case was almost two orders of magnitudes. Similar improvement was observed for the excited state, although, due to the low bond dimension the target state was lost again for certain interaction steps, i.e., for certain network configurations.

B. Locating avoided crossing by entanglement

Since the one- and two-orbital entropy functions were calculated to optimize network topologies they can also be used to locate the avoided crossing. For problems in condensed matter physics the one- and two-orbital entropy functions and the block entropy are used to locate quantum phase transitions^{52,53}. For translationally invariant systems the single-orbital entropy function is the same for all sites while in a chemical system it is orbital dependent. Therefore, the behavior of I_{tot} as a function of bond length can be used to detect and locate transition points where the wavefunction changes dramatically. In Fig. 15 I_{tot} is shown as a function of bond length. It can be seen that I_{tot} has a cusp like structure at $r = 11.86$ indicating the position of the avoided crossing.

IV. CONCLUSION

The present paper has been devoted to the application of the quantum-chemistry tree tensor network state (QC-TTNS) method to calculate the potential energy curve in

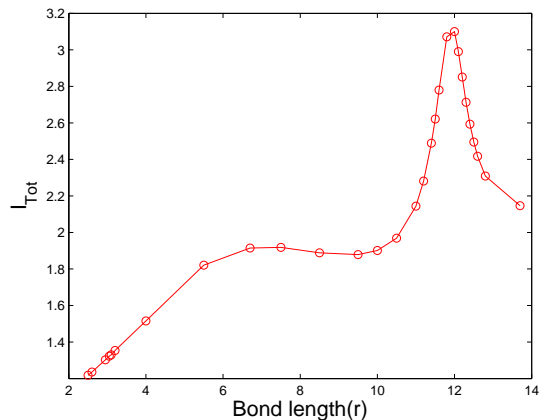


FIG. 15. (Color online) Total quantum information encoded in the wavefunction as a function bond length. The cusp-like structure indicates the dramatic change in the wavefunction.

the vicinity of the ionic-covalent avoided crossing in LiF. We have discussed the main features of the most general version of the QC-TTNS algorithm in which the local properties of the tensors can be different for each orbital. The optimized tensor topologies, which reflect the structure of the entanglement bonds between the molecular orbitals, were determined by minimizing the entanglement length in the system as the bond length between the Li and F was stretched. In order to compare tensor topology effects only, we have kept all parameters of the algorithms fixed and used a very small bond dimension or alternatively a very small number of block states. By compar-

ing the MPS(DMRG) and TTNS convergence properties we have demonstrated that the TTNS approach can converge to a significantly lower energy. Although the tensor contraction scales as D^{z+1} the TTNS topology offers a more optimal network structure since the relative error of the energy of the ground state as well as the excited states can be improved by an order of magnitude or more for the same value of D . This also indicates that the MPS result can be reproduced with a significantly lower bond dimension using the TTNS method.

Our QC-TTNS approach seems to be a promising direction reflected by the stability and fast convergence of the new method even for systems in which the wavefunction character changes as a function of bond length, especially in the region of an avoided crossing. In contrast to the MPS case, however, the optimization of the network is a more complex task. Extension of this work using more complex systems and orbital dependent coordination number is under progress.

ACKNOWLEDGMENTS

This research was supported by the European Research Area Chemistry (ERA-Chemistry) in part by the Hungarian Research Fund (OTKA) under Grant No. NN110360 and K100908, the DFG SCHN 530/9-1 project under Grant No. 10041620 and FWF-E1243-N19. V.M. and F.V. acknowledge support from the SFB-ViCoM project. Ö.L. acknowledges support from the Alexander von Humboldt foundation and from ETH Zürich during his time as a visiting professor. We are also grateful to Z. Rolik (Budapest) for providing his FCI code based on the CI algorithm of Olsen et al.⁴⁸.

-
- ¹ S. R. White, Phys. Rev. Lett. **69**, 2863–2866 (1992).
² S. R. White and R. L. Martin, J. Chem. Phys. **110**, 4127–4130 (1999).
³ Ö. Legeza, J. Röder and B. A. Hess, Molecular Physics **101**, 2019–2028 (2003).
⁴ G. K.-L. Chan, M. Kállay and G. Jürgen, J. Chem. Phys. **121**, 6110–6 (2004).
⁵ G. Moritz, B. A. Hess, M. Reiher, J. Chem. Phys. **122**, 024107, (2005).
⁶ Y. Kurashige and T. Yanai, J. Chem. Phys. **130**, 234114 (2009).
⁷ K. Boguslawski, P. Tecmer, G. Barcza, Ö. Legeza, and M. Reiher, J. Chem. Theory Comp. **9** 2959 (2013).
⁸ Ö. Legeza, R. Noack, J. Sólyom, and L. Tincani, in Computational Many-Particle Physics, eds. H. Fehske, R. Schneider, and A. Weisse **739**, 653–664 (2008).
⁹ K. H. Marti and M. Reiher, Z. Phys. Chem. **224**, 583–599 (2010).
¹⁰ G. K.-L. Chan and S. Sharma, Annu. Rev. Phys. Chem. **62**, 465–481 (2011).
¹¹ Ö. Legeza and J. Sólyom, Phys. Rev. B **68**, 195116 (2003),
¹² Ö. Legeza and J. Sólyom, Phys. Rev. B **70**, 205118 (2004).
¹³ J. Rissler, R.M.Noack, and S.R. White, Chemical Physics, **323**, 519 (2006).
¹⁴ G. Barcza, Ö. Legeza, K. H. Marti, and M. Reiher, Phys. Rev. A **83**, 012508 (2011).
¹⁵ K. Boguslawski, P. Tecmer, Ö. Legeza, and M. Reiher, J. Phys. Chem. Lett. **3**, 3129–3135 (2012).
¹⁶ Y. Kurashige, G. K.-L. Chan and T. Yanai, Nature Chemistry, DOI: 10.1038/NCHEM.1677 (2013).
¹⁷ S. Östlund and S. Rommer Phys. Rev. Lett. **75**, 3537 (1995).
¹⁸ F. Verstraete, J.I. Cirac, V. Murg, Adv. Phys. **57** (2), 143 (2008).
¹⁹ U. Schollwöck, Ann. Phys. (NY) **326**, 96 (2011).
²⁰ J. Haegeman, T. J. Osborne, and F. Verstraete, arXiv:1305.1894 (2013).
²¹ F. Verstraete and J. I. Cirac, arXiv:cond-mat/0407066v1 (2004).
²² V. Murg, F. Verstraete, and J. I. Cirac, Phys. Rev. A, **75**, 033605 (2007).
²³ V. Murg, F. Verstraete, and J. I. Cirac, Phys. Rev. B, **79**, 195119 (2009).
²⁴ G. Vidal, Phys. Rev. Lett., **101**, 110501 (2008)

- ²⁵ H. J. Changlani, J. M. Kinder, C. J. Umrigar, and G. K.-L. Chan, Phys. Rev. B, **80**, 245116 (2009).
- ²⁶ K. H. Marti, B. Bauer, M. Reiher, M. Troyer, and F. Verstraete, New J. Phys. **12** 103008 (2010).
- ²⁷ K. H. Marti, M. Reiher, Phys. Chem. Chem. Phys. **13** 6750-6759 (2011).
- ²⁸ Ö. Legeza, T. Röhwedder, and R. Schneider: Numerical approaches for high-dimensional PDE's for quantum chemistry, in Encyclopedia of Applied and Computational Mathematics, Editor-in-chief: Engquist, Björn ; Chan, T.; Cook, W.J.; Hairer, E.; Hastad, J.; Iserles, A.; Langtangen, H.P.; Le Bris, C.; Lions, P.L.; Lubich, C.; Majda, A.J.; McLaughlin, J.; Nieminen, R.M.; ODEEN, J.; Souganidis, P.; Tveito, A. (Eds.) Springer 2013 ISBN 978-3-540-70530-7
- ²⁹ Ö. Legeza, T. Rohwedder, R. Schneider, and Sz. Szalay, arXiv:1310.2736 (2013).
- ³⁰ W. Hackbusch, *Tensor Spaces and Numerical Tensor Calculus*, SSCM Vol. **42**, Springer, 2012.
- ³¹ R. Orus, arXiv:1306.2164 (2013).
- ³² V. Murg, F. Verstraete, Ö. Legeza, and R. M. Noack, Phys. Rev. B **82**, 205105 (2010).
- ³³ N. Nakatani and G. K.-L. Chan, J. Chem. Phys. **138**, 134113 (2013).
- ³⁴ Y. Shi, L. Duan, G. Vidal, Phys. Rev. **74**, 02232 (2006).
- ³⁵ L. Tagliacozzo, G. Evenbly, and G. Vidal, Phys. Rev. B **80**, 235127 (2009).
- ³⁶ P. Corboz and G. Vidal, Phys. Rev. B **80**, 165129 (2009).
- ³⁷ P. Corboz, G. Evenbly, F. Verstraete, and G. Vidal, Phys. Rev. A **81**, 010303(R) (2010).
- ³⁸ C. Lubich, T. Rohwedder, R. Schneider, B. Vandereycken, SIAM J. Matrix Anal. Appl. **34** 470-494 (2103)
- ³⁹ Ö. Legeza, J. Röder, and B. A. Hess, Phys. Rev. B **67**, 125114 (2003).
- ⁴⁰ I.P. Mcculloch, J. Stat. Mech., P10014 (2007).
- ⁴¹ A. I. Tóth, C. P. Moca, Ö. Legeza, and G. Zaránd, Phys. Rev. B **78**, 24510 (2008).
- ⁴² D. Zgid and M. Nooijen, J. Chem. Phys. **128**, 014107 (2008).
- ⁴³ S. Sharma and G. K.-L. Chan, J. Chem. Phys. **136**, 014107 (2012).
- ⁴⁴ S. Wouters, W. Poelmans, P. W. Ayers, and D. Van Neck, arXiv:1312.2415 (2013).
- ⁴⁵ U. Schollwöck, Rev. Mod. Phys. **77**, 259 (2005).
- ⁴⁶ C. W. Bauschlicher and S. R. Langhoff J. Chem. Phys., **89**, 4246-425 (1988).
- ⁴⁷ M.S.Gordon and M.W.Schmidt, "in: Theory and Applications of Computational Chemistry: the first forty years", 1167-1189, Elsevier, Amsterdam, (2005).
- ⁴⁸ J. Olsen and B. O. Roos and P. Jorgensen and H. J. Aa. Jensen, J. Chem. Phys., **89**, 2186 (1988).
- ⁴⁹ Ö. Legeza, F. Gebhard, and J. Rissler, Phys. Rev. B **74**, 195112 (2006).
- ⁵⁰ M. Fiedler, Czech. Math. Journal **23**, 298 (1973).
- ⁵¹ M. Fiedler, Czech. Math. Journal **25**, 619 (1975)
- ⁵² Ö. Legeza and J. Sólyom, Phys. Rev. Lett. **96**, 116401 (2006).
- ⁵³ Ö. Legeza, J. Sólyom, L. Tincani, and R. M. Noack, Phys. Rev. Lett. **99**, 087203 (2007).
- ⁵⁴ P. Tecmer, K. Boguslawski, O. Legeza, and M. Reiher, Phys. Chem. Chem. Phys. **16**, 719 (2014).
- ⁵⁵ O. Berkman and U. Vishkin, SIAM J. Comp. **22** (2): 221-242 (1993).